



Facile synthesis of single-nickel-atomic dispersed N-doped carbon framework for efficient electrochemical CO₂ reduction



Peilong Lu^{a,c}, Yijun Yang^b, Jiannian Yao^d, Meng Wang^{a,c}, Sobia Dipazir^{a,c}, Menglei Yuan^{a,c}, Jingxian Zhang^{a,c}, Xi Wang^b, Zhujun Xie^e, Guangjin Zhang^{a,*}

^a CAS Key Laboratory of Green Process and Engineering, Institute of Process Engineering, Chinese Academy of Science, 100190, Beijing, PR China

^b Key Laboratory of Luminescence and Optical Information, Ministry of Education, School of Science, Beijing Jiaotong University, 100044, Beijing, PR China

^c University of Chinese Academy of Science, 100049, Beijing, PR China

^d Beijing National Laboratory for Molecular Sciences (BNLMS), Institute of chemistry, Chinese Academy of Science, 100190, Beijing, PR China

^e School of Printing & Packaging, Beijing Institute of Graphic Communication, 102600, Beijing, PR China

ARTICLE INFO

Keywords:

CO₂ reduction

Single atom

Electrocatalysis

Carbon framework

Renewable energy

ABSTRACT

While converting carbon dioxide (CO₂) into value-added carbon products by electrolyzing offers a promising approach to mitigate global warming and store energy, poor selectivity and stability of catalysts still impede this conversion. Single-atom catalyst exhibits exceptional selectivity for CO₂ electroreduction reaction in response to inhibiting hydrogen evolution reaction (HER), which is the major obstacle to the development of CO₂ reduction. Herein we introduce a facile approach to obtain Ni-N_x sites encapsulating into carbon nanotubes with a nickel loading as high as 6.63 wt%. This catalyst exhibits high Faradaic efficiency approximately 95% for CO₂ electroreduction to carbon monoxide (CO) in the wide potential range from −0.7 to −1.0 V, and the current density reaches 57.1 mA cm^{−2} at −1.0 V versus a reversible hydrogen electrode (RHE). Experiments and characterization results demonstrate that nickel chemical state and content play a vital role for CO₂ electrocatalytic performance. Moreover, the simplifying of the synthesis may shed a new light on design single atom catalysts of electrochemistry in addition to CO₂ reduction.

1. Introduction

The even increasing global environmental crisis arouses more and more attention to greenhouse gases emission, conversion and storage [1–3]. Among all the challenges, the development of an artificial system that converts CO₂ into a kind of chemical energy with high efficiency is one of the major issues in modern chemistry. Electrochemical reduction of CO₂ is a desirable technology to achieve sustainable development, since it can not only mitigate the environmental effects of excessive emission of CO₂, but present a clean strategy for replacing fossil feedstock [4–8]. However, the conundrum of low efficiency, limited by competitive side reaction of hydrogen evolution reaction (HER) resulting from employing water as reaction medium, is still a major obstacle for further development of CO₂ reduction reaction (CO₂RR) [9,10]. Thus, design of novel electrocatalyst composed of earth abundant elements with high activity and selectivity is pivotal for realizing CO₂ electroreduction.

Over the past few years, researchers have designed various kinds of catalysts, such as metals, metal alloys, metal oxides, metal

chalcogenides and carbon-based materials, to test their performance on CO₂RR [11–18]. Recently, single-atomic Ni doped carbon materials were found to exhibit excellent activity and selectivity on CO₂RR [9,10,19–25]. Li et al prepared a single atomic Ni containing catalyst with a Faradaic efficiency for CO production of over 71.9% [21]. Wu et al successfully synthesized Ni-N₄ structure with extremely high selectivity for CO (Faradaic efficiency of 99% at −0.81 V) [10]. However, the synthesis route of the Ni-N₄ structure is complicated and need many steps with low yield, which limited their scale up and application in real industries. Thus to development of such single-atomic electrocatalyst with both simple synthesis route and high activity/selectivity remains challenges.

Herein, we developed a facile approach to synthesis of single-nickel-atomic dispersed N-doped carbon nanotubes (Ni SAs/NCNTs) with promising high activity and selectivity for CO₂RR. The catalyst was obtained by simply pyrolysis of the mixture of small organic molecules (Dicyandiamide and 2-methylimidazole) with Zn/Ni salts, with a Ni loading as high as 6.63 wt%. The obtained catalyst can achieve high Faradaic efficiency (FE) over 95% for CO in wide potential range from

* Corresponding author.

E-mail address: zhanggj@ipe.ac.cn (G. Zhang).

−0.7 to −1.0 V and gives a maximum FE of 97% at −0.9 V with a current density of 41.5 mA cm^{−2}. (All potential are in reference to the RHE) The catalyst also exhibit good stability which maintained FE of around 90% during electrolyzing over 30 h.

2. Experiment

2.1. Materials

Analytical grade Zinc nitrate hexahydrate ($Zn(NO_3)_2 \cdot 6H_2O$), Nickel chloride hexahydrate ($NiCl_2 \cdot 6H_2O$), Iron chloride tetrahydrate ($FeCl_2 \cdot 4H_2O$), Tin chloride dihydrate ($SnCl_2 \cdot 2H_2O$), Manganese chloride tetrahydrate ($MnCl_2 \cdot 4H_2O$), Cobalt chloride hexahydrate ($CoCl_2 \cdot 6H_2O$), Potassium bicarbonate ($KHCO_3$) and Methanol anhydrous (CH_3OH) were acquired from XIOLONG SCIENTIFIC, China. 2-Methylimidazole ($C_4H_6N_2$) and Dicyandiamide ($C_2H_4N_4$) were obtained from Aladdin. Nafion® 117 solution was purchased from Sigma-Aldrich. All of those chemical used in the experiment without further purification except carbon cloth (CC). In a typical procedure, hydrophilic CC was acquired through refluxing it in concentrated HNO_3 at 100 °C for 2 h. After cleaned with ethanol and water, CC was dried under Ar for overnight. Ultrapure water from Millipore system (Millipore, Billerica, MA) was used in all the procedure of experiments.

2.2. Characterization

Scanning electron microscope (SEM) images was performed by SU8020 (Hitachi Japan) operated at an acceleration voltage of 50 kV. Field-emission high resolution transmission electron microscope (TEM) and the corresponding energy dispersive spectroscopy mapping analyses were carried out on JEM-2100F at an acceleration voltage of 200 kV. The high-angle annular dark-field scanning transmission electron microscope (HAADF-STEM) was performed on JEOL JEM-ARM200F TEM/STEM with a spherical aberration corrector. The X-ray powder diffraction (XRD) patterns were obtained by Bruker AXS D advance powder diffractometer equipped with a Cu K α ($\lambda = 0.15418$ nm). X-ray photoelectron spectroscopy (XPS) measurements were conducted by ultrahigh vacuum (HUV) with a Krato, AXIS-HS monochromatized Al K α cathode source, at 75–150 W, using a low energy electron gun for charge neutralization. Differential scanning calorimeter-thermogravimetric analysis (DSC-TGA) was carried out on TA SDT Q600. Raman spectra were recorded on Renishaw inVia with wavelength of 532 nm. The liquid products were quantified by nuclear magnetic resonance (NMR) (Bruker AVANCE AV III 600) spectroscopy using Deuterium oxide as an internal standard. The gas products were analyzed by gas chromatograph (SP-6890) in 1 h intervals to detect the concentration of gas products during chronoamperometry. Nitrogen sorption isotherms were measured on Quantachrome Autosorb-IQ at 77 K with N_2 physical adsorption, and the specific surface area was obtained by the Brunauer-Emmett-Teller (BET) method. The pore volumes and pore size distribution were calculated by the Discrete-Fourier-Transformation (DFT) method.

2.3. Catalyst preparation

2.3.1. Synthesis of Ni SAs/NCNTs

0.837 g $Zn(NO_3)_2 \cdot 6H_2O$ and a certain amount of $NiCl_2 \cdot 6H_2O$ (0.1 mmol, 0.3 mmol and 0.5 mmol) were dissolved in 35 mL methanol first. 2 g dicyandiamide (DCD) and 0.924 g 2-methylimidazole (2-MeIm) were added into above solution in sequence under vigorously stirring at room temperature overnight (more than 8 h). After evaporation of methanol from the mixture at 50 °C, the as-obtained solid was washed with methanol and dried at 60 °C overnight. Then, the dried solid was pyrolyzed at a certain temperature (700, 800, 900, and 1000 °C) for 2 h at a heating rate of 5 °C min^{−1} under flow of Ar. With an amount of 0.3 mmol $NiCl_2 \cdot 6H_2O$ in the synthesis route, the Ni SAs/

NCNTs was obtained at 1000 °C.

2.3.2. Synthesis of Ni/ZIF

Similarly, 0.837 g $Zn(NO_3)_2 \cdot 6H_2O$ and 71.3 mg (0.3 mmol) $NiCl_2 \cdot 6H_2O$ were dissolved in 35 mL methanol. Then 0.924 g 2-MeIm was added into above solution under vigorously stirring at room temperature overnight. After evaporation of methanol from the mixture at 50 °C, the as-obtained solid was washed with methanol and dried at 60 °C overnight. At last, the dried solid was pyrolyzed at 1000 °C for 2 h at a heating rate of 5 °C min^{−1} under flow of Ar to yield Ni/ZIF.

2.3.3. Synthesis of Ni/DCD

Similarly, 71.3 mg (0.3 mmol) $NiCl_2 \cdot 6H_2O$ was dissolved in 35 mL methanol. Then 2 g dicyandiamide (DCD) was added into nickel chloride solution under vigorously stirring overnight at room temperature. After evaporating methanol at 50 °C, the as-obtained solid was washed with methanol and dried at 60 °C overnight. At last, the dried solid was pyrolyzed at 1000 °C for 2 h at a heating rate of 5 °C min^{−1} under flow of Ar to yield Ni/DCD.

2.3.4. Synthesis of N-C

Similarly, 0.837 g $Zn(NO_3)_2 \cdot 6H_2O$ was dissolved in 35 mL methanol. 2 g DCD and 0.924 g 2-MeIm were added into above zinc nitrate solution under vigorously stirring overnight at room temperature. After evaporation of methanol from the mixture at 50 °C, the as-obtained solid was washed with methanol and dried at 60 °C overnight. At last, the dried solid was pyrolyzed at 1000 °C for 2 h at a heating rate of 5 °C min^{−1} under flow of Ar to yield N-C.

2.3.5. Synthesis of Fe, Sn, Co and Mn decorated catalysts

Similarly, 0.837 g $Zn(NO_3)_2 \cdot 6H_2O$ and 0.3 mmol $MeCl_x \cdot xH_2O$ (Me: Fe, Sn, Co, and Mn) were dissolved in 35 mL methanol first. 2 g dicyandiamide (DCD) and 0.924 g 2-methylimidazole (2-MeIm) were added into above solution in sequence under vigorously stirring at room temperature overnight (more than 8 h). After evaporation of methanol from the mixture at 50 °C, the as-obtained solid was washed with methanol and dried at 60 °C overnight. Then, the dried solid was pyrolyzed at 1000 °C for 2 h at a heating rate of 5 °C min^{−1} under flow of Ar. The obtained catalysts were simply denoted as Fe, Sn, Co, and Mn.

2.4. Electrochemical measurements

The electrochemical measurements were performed with electrochemical workstation (CHI660E). CO₂RR was carried out in a custom-made two-compartment tight electrolytic cell, which was separated by cation exchange membrane (Nafion 117 membrane) (Fig. S1) (Supplementary Information). Each compartment contained 80 mL electrolyte (0.5 M KHCO₃). The solution of cathode was purged with 30 mL min^{−1} CO₂ (> 99.999%) until saturated (pH = 7.2). Catalytic performance tests were carried out under chronoamperometry for 1 h. The working electrode was prepared by loading 160 μL of the homogenous ink, which dispersing 2.5 mg sample and 20 μL Nafion solution (5 wt. %) in 480 μL ethanol solution by sonicating for 1 h, onto the two sides of a carbon cloth with 1 cm² (1 × 0.5 cm), giving a catalyst loading of 0.8 mg cm^{−2}. The reference and counter electrodes used were saturated calomel electrode (SCE) and platinum wire, respectively. For CO₂ reduction experiments, linear sweep voltammetry (LSV) with 50 mV s^{−1} was performed in CO₂-saturated electrolyte stirred at 400 rpm. All LSV curves were corrected by ohmic compensation (~10 Ω in CO₂-saturated 0.5 M KHCO₃), and all current densities were calculated to the geometrical area of electrode. The Tafel slope was calculated according to Tafel equation as following:

$$\eta = b \log \left(\frac{J}{J_0} \right)$$

Where η is overpotential, b is Tafel slope, J_{CO} is current density of CO,

and J_0 is the exchange current density.

Gas products were detected by gas chromatograph (GC). In detail, H_2 was measured by thermal conductivity detector (TCD) and CO was analyzed by flame ionization detector (FID). Liquid products were measured by nuclear magnetic resonance (NMR).

The potential in this paper was converted to reversible hydrogen electrode by the following equation (Nernst equation, at 25 °C):

$$E \text{ (vs. RHE)} = E \text{ (vs. SCE)} + 0.244 \text{ V} + 0.059 \times \text{pH}$$

The faradaic efficiency (FE) of H_2 and CO were calculated by using the concentrations (ppm) detected by the gas chromatograph as follows:

$$\text{FE}_x = \frac{\text{ppm} \times \text{flow rate} \times nFp_0/\text{RT}}{J_{\text{Total}}} \times 100\%$$

Where $n = 2$ is the number of electrons transferred CO_2 to a given product; p_0 is atmospheric pressure and the $T = 372.15 \text{ K}$. 10 mL min^{-1} of CO_2 flow rate was used in this measurement. F is Faraday constant, having value $96,485 \text{ C mol}^{-1}$. J_{Total} is the total current density. $R = 22.4 \text{ L mol}^{-1}$ is the gas constant. Similarly, the partial current densities could be calculated as follows:

$$J_x = \frac{\text{ppm} \times \text{flow rate} \times nFp_0/\text{RT}}{\text{geometric surface area}}$$

Electrochemically active surface area (ECSA) was calculated based on the definition:

$$\text{ECSA} = C_{dl}/C_s$$

Where C_{dl} corresponds to the slope of the double-layer charging current versus the scan rate plot, and the value of C_s we used is $40 \mu\text{F cm}^{-2}$.

The turnover frequency (TOF, hour $^{-1}$) of CO was computed as follows:

$$\text{TOF} = \frac{J_{co} \times \text{geometric surface area}/nF}{\omega m_{\text{catalyst}}/M_{Ni}}$$

Where ω is the content of Ni in the catalyst (wt%, measured by ICP-OES); m_{catalyst} is the catalyst mass dispersed on carbon cloth as working electrode, and $M_{Ni} = 58.69 \text{ g mol}^{-1}$ is the relative atomic mass of Ni.

3. Results and discussion

3.1. Preparation and morphology of sing-nickel-atom catalyst

For preparation of the target catalyst, the simple synthesis route was developed. As shown in Fig. 1a, certain amount of Dicyandiamide (DCD) and 2-Methylimidazole (2-MeIm) were mixed with $NiCl_2 \cdot 6H_2O$, $Zn(NO_3)_2 \cdot 6H_2O$ in methanol intensively at room temperature. During the synthesis, Zn^{2+} can react with 2-MeIm to form ZIF-8 [26]. Then DCD and Ni^{2+} was either absorbed or attached on the crystalline of ZIF-8. As shown in Fig. S3, the obtained powder (Fig. S2) of ZIF-8/DCD/ Ni^{2+} by evaporation of methanol from the mixture after reaction remains the typical morphology of ZIF-8 structure. This solid was further pyrolyzed at 800–1000 °C under the protection of Ar to get the products named as Ni SAs/NCNTs. For comparison, the samples obtained by pyrolysis of ZIF-8/ Ni^{2+} (mixture of ZIF-8 and Ni salt) and DCD/ Ni^{2+} (mixture of DCD and Ni salt) with same reaction condition were also prepared to demonstrate the role ZIFs and DCD in the final catalyst and were named as Ni/ZIF and Ni/DCD respectively.

The catalysts were firstly characterized by scanning electron microscope (SEM), transmission electron microscopy (TEM), as well as high-angle annular dark-field scanning transmission electron microscope (HAADF-STEM). As shown in Fig. 1b, the bamboo-like carbon nanotubes interweaving with irregular nanostructures were observed. There are no ZIFs structure remained indicating its conversion to carbon skeleton during pyrolysis. TEM image and corresponding energy-dispersive X-ray spectroscope (EDS) analysis, shown in Fig. 1c,

indicate that both the Ni and N were dispersed evenly in these carbon nanotubes over the whole structure (Fig. S4). More importantly, HAADF-STEM images of Ni SAs/NCNTs showed that the Ni atoms, which are marked with red circles, distributed homogeneously on the surface of carbon nanotubes and dominantly exhibit the atomic dispersion (Fig. 1d, e), although some of small Ni nanoparticles with size of 2–4 nm were observed on the carbon nanotubes (Fig. S5). In the case, it is worth to mention that Zn would be evaporated away due to its relative low molten point (420 °C) and boiling point (907 °C). In fact, the content of Zn in Ni SAs/NCNTs, measured by inductively coupled plasma optical emission spectroscopy (ICP-OES), is around 0.37 wt%, which is pretty much lower than 6.63 wt% of Ni content (Table S2). Also, there is no signal of Zn element detected by EDS analysis (Fig. S4). All of these results verified that these bright dots virtually derived from Ni atoms rather than Zn. As for Ni/ZIF and Ni/DCD, large amount of Ni particles were observed in TEM images (Fig. S6).

3.2. Electrocatalytic CO_2RR performance

The electrocatalytic performance of prepared catalyst was first evaluated by linear sweep voltammetry (LSV). As shown in Fig. 2a, in CO_2 saturated $KHCO_3$ solution, Ni SAs/NCNTs exhibited the onset potential of about -0.5 V and achieved the total current density of 57.1 mA cm^{-2} at -1.0 V , indicating remarkable excellent activity. In contrast, in spite of the existence of Ni, Ni/ZIF showed moderate activity and Ni/DCD as well as the sample obtained by pyrolyzing of mixture of DCD and ZIF-8 (without Ni doped, denoted as N-C) showed poor activity. The measurement of Faradaic efficiency by recording the concentrations of gas products was carried out after one-hour of electrolysis at given potentials. Only CO and H_2 were detected in the products and no liquid product produced, verified by ^1H nuclear magnetic resonance (Fig. S7). Ni SAs/NCNTs attained a stable FE for CO up to 95% when the potential was higher than 0.7 V (Fig. 2b) and the maximum FE for CO can reach 97% at potential of -0.9 V . While for the other catalysts, Ni/ZIF showed close FE values with that of Ni SAs/NCNTs at relatively low potential range (-0.5 to -0.7 V). However, its FE for CO decreased significantly at high potential range (-0.8 to -1.0 V), while HER was becoming stronger (Fig. S8), indicating inadequate reactive sites available for CO_2RR under over high current density. The other two catalysts of Ni/DCD and N-C shared the most sluggish activity with FE for CO below 10%.

In addition, Tafel slopes were analyzed to determine the kinetics of CO_2RR on different catalysts. As shown in Fig. 2c, the Ni SAs/NCNTs exhibits the lowest Tafel slope (127 mV/dec), which is much smaller than that of Ni/ZIF (410 mV/dec), Ni/DCD (636 mV/dec), and ZIF/DCD (442 mV/dec), indicating favorable kinetics for the formation of CO. While in N_2 -saturated $KHCO_3$ solution (pH = 9.03), current density of Ni SAs/NCNTs is much smaller than that in CO_2 -saturated solution (Fig. S9), demonstrating the high activity of Ni SAs/NCNTs indeed derives from CO_2 reduction. Long-term stability of Ni SAs/NCNTs was tested under potential of -0.75 V . Both the FE for CO and the current density showed little decay during 30 h of operation, indicating the high stability of the prepared catalyst (Fig. 2d). The TOF was calculated to be 1176 h^{-1} based on the Ni site, with the potential of -1.0 V .

3.3. Structural characterization

To the best of our knowledge, this catalytic behavior suppressed those of most of the recent reported catalysts (Table S1). To uncover the main reason of the high catalytic performance of Ni SAs/NCNTs, series characterizations were carried out. The prepared catalysts were firstly characterized by X-ray diffraction (XRD), showed in Fig. 3a. Ni SAs/NCNTs and Ni/ZIF showed two small weak diffraction peaks at 44.3° and 51.7° attributed to (111) and (200) crystal facets from the face-centered-cubic Ni phase (PDF#87-0712), indicating formation of Ni nanoparticles that is in accordance with the TEM observations (Figs. S5,

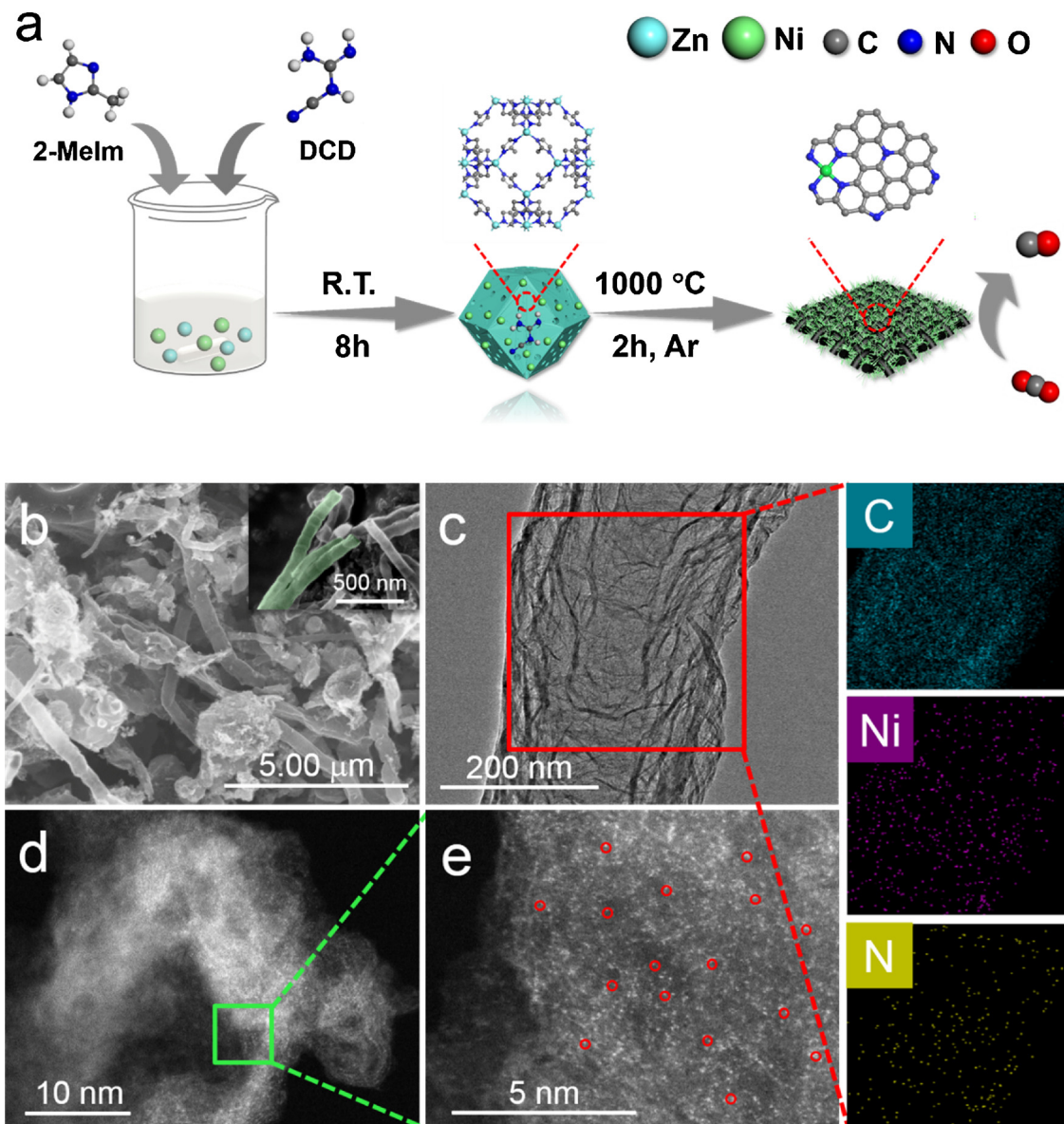


Fig. 1. (a) Scheme for the synthesis of Ni SAs/NCNTs. (b) SEM, (c) TEM images of Ni SAs/NCNTs, corresponding element maps showing the distribution of Ni (purple) and N (yellow) across the entire carbon support (blue). (d, e) Magnified HAADF-STEM images of Ni SAs/NCNTs. The Ni single atoms are marked with red circles. (For interpretation of the references to colour in this figure legend, the reader is referred to the web version of this article.)

S6). While for Ni/DCD, strong diffraction peaks of Ni can be observed, suggesting large amount of Ni nanoparticles appeared in this sample. Notably, all catalysts present characteristic peak at approximately 24° corresponding to (002) plane of graphite (PDF#75-1621). Furthermore, Raman spectra in Fig. S10 also verified the formation of graphene for Ni SAs/NCNTs and N-C clearly.

The porosity of the Ni SAs/NCNTs was analyzed by BET in Fig. 3b, revealing the presence of high density of pores in the material with a high specific surface area. A clear hysteresis loop of type 1 V is formed for BET analysis of the material with a specific surface area SBET of 689 m² g⁻¹, while the total pore volume of the material comes out to be 1.0 cc g⁻¹ and the average pore size calculated by density functional theory (DFT) is 1.475 nm (inset of Fig. 3b). In contrast, Ni/ZIF and Ni/DCD shared similarly low SBET. In addition, the electrochemical active surface area (ECSA) was measured to illustrate the excellent electrochemical performance of Ni SAs/NCNTs. The slope in Fig. S11, which was derived from measurement of double-layer capacitance, could be a reference of ECSA [27]. The consequence demonstrated that the ECSA of Ni SAs/NCNTs and N-C were much larger than Ni/ZIF and Ni/DCD,

indicating sufficient area to support reactive sites for Ni SAs/NCNTs. Theoretically, for Ni SAs/NCNTs, its higher surface area is one of the most important attributes that sharply improves the catalytic performance for CO₂RR.

The chemical composition and elemental state in the catalyst is further analyzed by XPS. The orbital peaks of the XPS survey spectrum divulge the presence of Ni, N, C and O elements (Fig. S12). Fig. 3c shows main elemental content of Ni SAs/NCNTs, and Ni SAs/NCNTs has higher N content (5.22 at%) compared with Ni/ZIF (4.22 at%) and Ni/DCD (3.05 at%). In Ni SAs/NCNTs, the deconvolution of N 1 s high-resolution profile shows five peaks corresponding to pyridinic, Ni-N, pyrrolic, quaternary, and oxidized centered at 398.2 eV, 399.2 eV, 400.6 eV, 401.3 eV and 403.0 eV respectively (inset of Fig. 3c) [9]. The loading of Ni is to be 6.63 wt%, evaluated by ICP-OES, which is more than 3 times as high as Ni/ZIF (2.01 wt%). That explains the low activity (current density) of Ni/ZIF and the downturn of FE under high applied potential. The binding energies of Ni 2p_{3/2} in Ni SAs/NCNTs and Ni/ZIF were about 854.7 and 855.0 eV, respectively (Fig. 3d), which are nearly 1.0 eV lower than that of Ni²⁺ in nickel

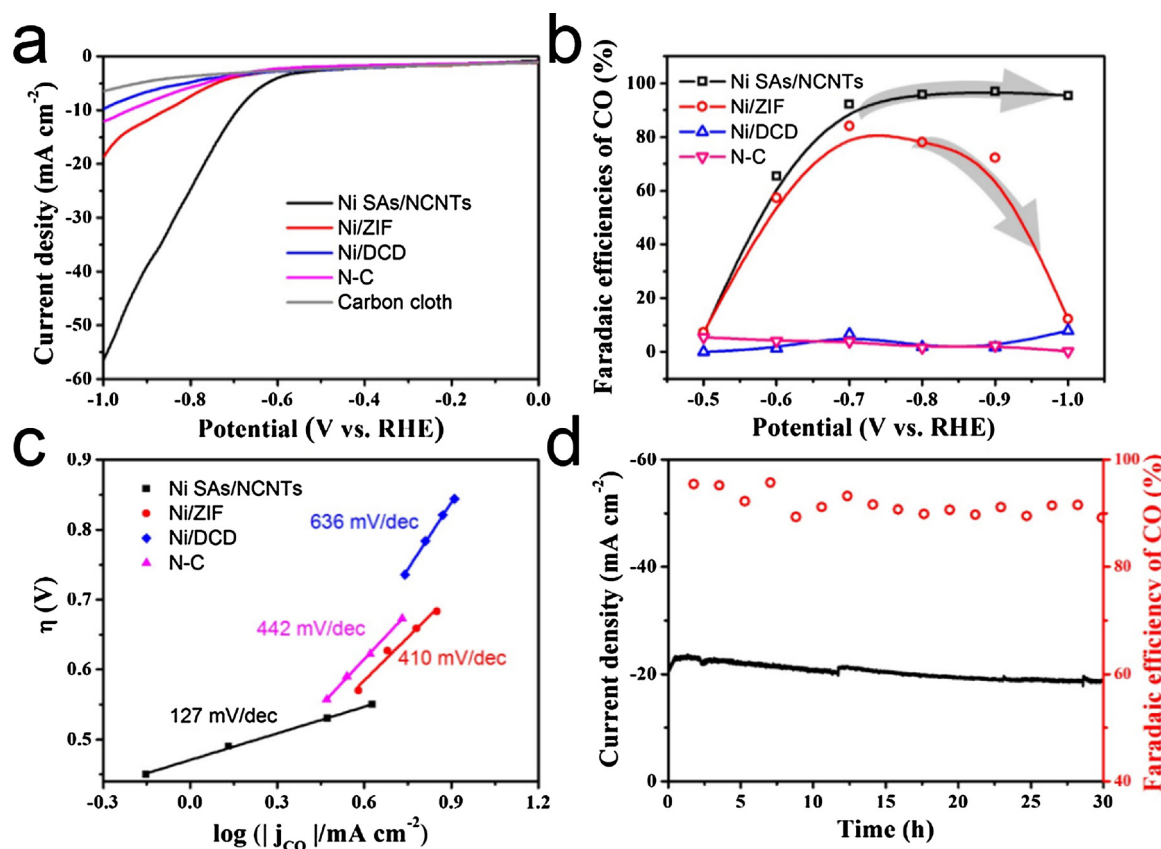
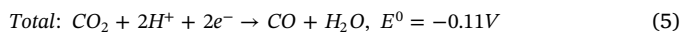


Fig. 2. (a) Linear sweep voltammetric curves, and pure carbon cloth servers as background. (b) Faradaic efficiencies of CO at different applied potentials. (c) Tafel plots for producing CO. (d) Catalytic stability test of Ni SAs/NCNTs at -0.75 V for 30 h.

phthalocyanine (Ni Pc, Fig. S13) (856.0 eV). In Ni/DCD, the Ni $2p_{3/2}$ deconvoluted into two peaks. The minor peak at 852.6 eV, which corresponds to metallic Ni⁰, and there is a major peak at 854.0 eV, which is about 1 eV lower than Ni SAs/NCNTs or Ni/ZIF. Thus, the XPS results of Ni $2p_{3/2}$ reveal that Ni atoms in Ni SAs/NCNTs and Ni/ZIF are likely to be in a high-valent state but lower than +2. As a result, the existence of large quantity of Ni-Nx sites anchored on carbon can result in the high selectivity of CO₂RR, which have been demonstrated before. In our case, although there is some small Ni NPs formed in the materials, the abundant Ni-Nx sites suppressed the hydrogen evolution activity induced by Ni NPs. Therefore, a typical electroreduction process of CO₂ is illustrated. The initial electron transfer reaction for CO₂ activation to $^{*}\text{CO}_2^{-}$ intermediate (Eq. (1)) in Ni SAs/NCNTs have been regarded as a rate-determining step, and Ni-Nx site can be easier to form $^{*}\text{CO}_2^{-}$ [21]. As shown in following equations, the obtained $^{*}\text{CO}$ intermediate is weak to bond with Ni-Nx sites and thus escapes as CO gas (* represents the site that intermediate can bond with catalyst).



Due to the Ni SAs/NCNTs exhibits abundant low-coordinated sites, the strong bonding with CO₂⁻ may result in the excellent performance for CO₂ electroreduction. Moreover, the increased number of exposed active sites, strengthened electronic conductivity, and lower adsorption energy of CO over the Ni-Nx sites. All of these may contribute to the improved CO₂ electrocatalytic performance of Ni SAs/NCNTs.

The pyrolysis of Ni/ZIF/DCD was clearly tracked by

thermogravimetric analysis (TGA). As shown in Fig. S14, there are three typical weight loss at about 200 °C, 312 °C and 702 °C respectively. The former two weight losses were attributed to loss of crystalline water and decomposition of the mixture of ZIF-8 and DCD, respectively [21]. When the temperature was elevated to over 702 °C, a remarkable endothermic process was observed indicating a key process happens at this temperature. SEM and TEM observations showed that the samples pyrolyzed at 700 °C exhibit irregular morphology and no carbon nanotubes can be observed. Whereas, for samples annealed at higher temperature (800, 900 and 1000 °C), they all show very close morphology with lots of carbon nanotubes (Fig. S15). Electrolycatalytic experiment proved that the samples obtained at 800 °C and 900 °C showed similar activity and selectivity to that obtained at 1000 °C. Whereas the sample pyrolyzed at 700 °C showed extremely sluggish activity to CO₂RR (Fig. S16). This results is interesting since according to Li et al., only when the temperature is above 907 °C which is boiling point of Zn, the single Ni atomic dispersed carbon materials can be obtained with good activity, since it is believed that Ni²⁺ can occupied the vacancy induced by evaporation of Zn [21]. However, in the case, even at much lower temperature, high quality of Ni SAs/NCNTs can also be obtained. XRD in Fig. S17 showed that at 800 °C, a new phase of Ni₃ZnC (PDF#28-0713) can even be detected instead of Ni NPs. The catalytic result indicates that the existence of Zn does not affect the activity of the prepared catalyst. This means the annealing temperature can be decreased significantly by our new synthesis strategy.

3.4. Discussion

In our synthesis strategy, we have introduced three components, ZIF-8, DCD and Ni²⁺. Experiment results indicate the entire three components are necessary to get high quality of the catalyst. The comparison experiment showed that bi-component catalyst exhibited

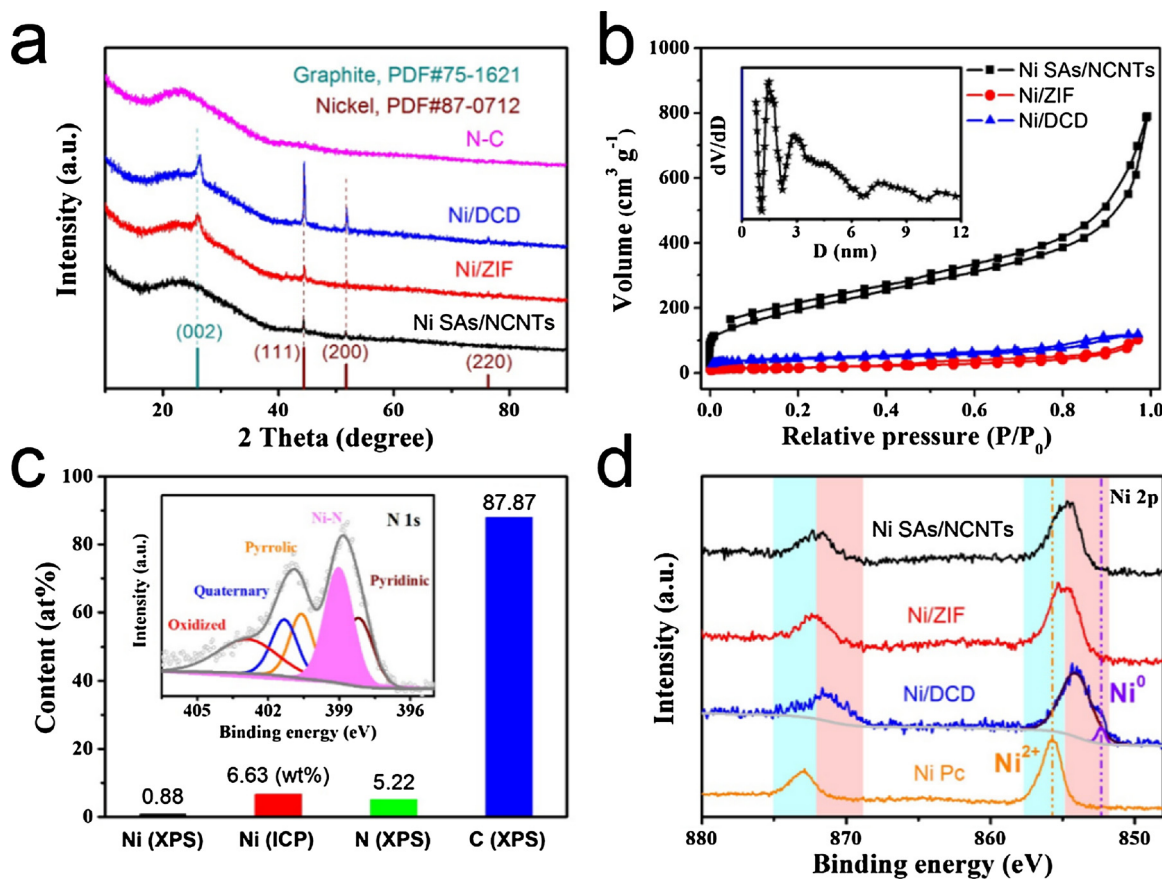


Fig. 3. (a) XRD patterns. The PDF profiles of graphite (green) and metallic nickel (brown) are displayed for reference. (b) N₂ adsorption and desorption isotherms; inset: the pore size distribution of Ni SAs/NCNTs. (c) Elemental content of Ni SAs/NCNTs, obtained from XPS and ICP-OES measurements; inset: the high resolution XPS N 1s spectrum. (d) High resolution XPS Ni 2p spectra. (For interpretation of the references to colour in this figure legend, the reader is referred to the web version of this article.)

much lower activities to CO₂RR (Fig. 2a, b). For Ni/ZIF, although it showed close activity to that of Ni SAs/NCNTs at low overpotential, the sharp decrease of its activity under high overpotential suggests that there is not enough active site for CO₂RR. TEM analysis found that there are lots of large Ni NPs can be observed in this samples (Fig. S6). As for Ni/DCD, only bamboo-like carbon nanotubes can be obtained with this sample which showed poor activity for CO₂RR (Figs. 2b, S6). In this case, Ni²⁺ was reduced at high temperature to form Ni NPs with good crystallization. These Ni NPs catalyzed growth of carbon nanotubes at elevated temperature. Based on all these observations, a possible mechanism of forming Ni SAs/NCNTs was proposed. Firstly, Ni²⁺ can be absorbed within the pores of ZIF-8. DCD have no direct interaction with Ni²⁺ and ZIF-8 at the beginning. At elevated temperature, DCD transformed to some cyclic azines structure, as shown in Fig. S18, which could lead to the tubular structures [28]. The final product of self-reaction of DCD melon is unreactive till 700 °C. At same time, ZIF-8 also experienced structure decomposition that may release absorbed Ni²⁺ outside. These released Ni²⁺ can quickly be trapped by strong coordination ability of pyrolyzed product of DCD which is rich of pyridinic N to form a large quantity of Ni-Nx-C sites. Some un-trapped Ni²⁺ was reduced to form Ni NPs and they can serve as the catalyst for growth of carbon nanotubes. Thus at last Ni SAs/NCNTs was obtained by a series of complicated reaction during high temperature treatments.

Furthermore, the effect of different Ni loading in Ni SAs/NCNTs was explored. By controlling the original use of Ni in precursor, as shown in Fig. S19, series of catalysts were obtained. However, their catalytic performance did not be affected obviously (Fig. S20). In contrast, XRD patterns show that the catalysts hold increasing crystallinity with the enhancing content of Ni, and the results of ICP-OES indicate that the

loading of Ni in these catalysts are to be 4.04 wt%, 6.63 wt%, and 7.18 wt%, respectively. All of these evidences verify that the Ni particles in our materials plays a minor role for CO₂RR.

In addition, inspired by Ni SAs/NCNTs' outstanding catalytic performance and characterization, we have measured some of other metal-doped catalysts synthesized by the same route, such as Mn, Sn, Fe and Co (Fig. S21). However, they hardly have catalytic performance for CO₂RR except for Fe, since the vigorous hydrogen evolution reaction seriously consumes the majority of electricity. Therefore, in our strategy, nickel is the best metal to synthesize the catalyst for CO₂ electroreduction based on our observations.

4. Conclusion

In this study, we have successfully developed a facile synthetic route for large scale preparation of single Ni atomic dispersed carbon materials with pretty high selectivity and stability toward CO₂ reduction. The prepared catalyst gives a maximum FE of 97% at -0.9 V with a current density of 43.5 mA cm⁻². This facile synthesis strategy and excellence electrocatalytic performance may pave a new path for design of high-efficiency catalysts to CO₂ reduction.

Conflicts of interest

There are no conflicts to declare.

Acknowledgements

This work was supported by the National Natural Science

Foundation of China (No. 91545125 and U1662121), Beijing Municipal Commission of Education (KM201710015009), and Cross training plan for high level talents in Beijing colleges and universities.

Appendix A. Supplementary data

Supplementary material related to this article can be found, in the online version, at doi:<https://doi.org/10.1016/j.apcatb.2018.09.025>.

References

- [1] E. Anagnostou, E.H. John, K.M. Edgar, G.L. Foster, A. Ridgwell, G.N. Inglis, R.D. Pancost, D.J. Lunt, P.N. Pearson, Changing atmospheric CO₂ concentration was the primary driver of early Cenozoic climate, *Nature* 533 (2016) 380.
- [2] B. Obama, The irreversible momentum of clean energy, *Science* 355 (2017) 126–129.
- [3] Y. Mun, K. Kim, S. Kim, S. Lee, S. Lee, S. Kim, W. Choi, S.-k. Kim, J.W. Han, J. Lee, A novel strategy to develop non-noble metal catalyst for CO₂ electroreduction: Hybridization of metal-organic polymer, *Appl. Catal. B: Environ.* 236 (2018) 154–161.
- [4] S. Gao, Y. Lin, X. Jiao, Y. Sun, Q. Luo, W. Zhang, D. Li, J. Yang, Y. Xie, Partially oxidized atomic cobalt layers for carbon dioxide electroreduction to liquid fuel, *Nature* 529 (2016) 68.
- [5] M. Liu, Y. Pang, B. Zhang, P. De Luna, O. Voznyy, J. Xu, X. Zheng, C.T. Dinh, F. Fan, C. Cao, F.P.G. de Arquer, T.S. Safaei, A. Mepham, A. Klinkova, E. Kumacheva, T. Fileteer, D. Sinton, S.O. Kelley, E.H. Sargent, Enhanced electrocatalytic CO₂ reduction via field-induced reagent concentration, *Nature* 537 (2016) 382.
- [6] J.-H. Kim, H. Woo, S.-W. Yun, H.-W. Jung, S. Back, Y. Jung, Y.-T. Kim, Highly active and selective Au thin layer on Cu polycrystalline surface prepared by galvanic displacement for the electrochemical reduction of CO₂ to CO, *Appl. Catal. B: Environ.* 213 (2017) 211–215.
- [7] Z. Li, Y. Jiang, C. Liu, Z. Wang, Z. Cao, Y. Yuan, M. Li, Y. Wang, D. Fang, Z. Guo, D. Wang, G. Zhang, J. Jiang, Emerging investigator series: dispersed transition metals on a nitrogen-doped carbon nanoframework for environmental hydrogen peroxide detection, *Environ. Sci. Nano* 5 (2018) 1834–1843.
- [8] J.-F. Chen, Green chemical engineering for a better life, *Engineering* 3 (2017) 279.
- [9] H.B. Yang, S.-F. Hung, S. Liu, K. Yuan, S. Miao, L. Zhang, X. Huang, H.-Y. Wang, W. Cai, R. Chen, J. Gao, X. Yang, W. Chen, Y. Huang, H.M. Chen, C.M. Li, T. Zhang, B. Liu, Atomically dispersed Ni(i) as the active site for electrochemical CO₂ reduction, *Nat. Energy* 3 (2018) 140–147.
- [10] X. Li, W. Bi, M. Chen, Y. Sun, H. Ju, W. Yan, J. Zhu, X. Wu, W. Chu, C. Wu, Y. Xie, Exclusive Ni-N₄ sites realize near-unity CO selectivity for electrochemical CO₂ reduction, *J. Am. Chem. Soc.* 139 (2017) 14889–14892.
- [11] D.D. Zhu, J.L. Liu, S.Z. Qiao, Recent advances in inorganic heterogeneous electrocatalysts for reduction of carbon dioxide, *Adv. Mater.* 28 (2016) 3423–3452.
- [12] C.W. Li, M.W. Kanan, CO₂ reduction at low overpotential on Cu electrodes resulting from the reduction of thick Cu₂₀ films, *J. Am. Chem. Soc.* 134 (2012) 7231–7234.
- [13] S. Rasul, D.H. Anjum, A. Jedidi, Y. Minenkov, L. Cavallo, K. Takanabe, A highly selective copper-indium bimetallic electrocatalyst for the electrochemical reduction of aqueous CO₂ to CO, *Angew. Chem.-Int. Ed.* 54 (2015) 2146–2150.
- [14] S. Sarfraz, A.T. Garcia-Esparza, A. Jedidi, L. Cavallo, K. Takanabe, Cu-Sn bimetallic catalyst for selective aqueous electroreduction of CO₂ to CO, *ACS Catal.* 6 (2016) 2842–2851.
- [15] G.O. Larrazabal, A.J. Martin, S. Mitchell, R. Hauert, J. Perez-Ramirez, Enhanced reduction of CO₂ to CO over Cu-In electrocatalysts: catalyst evolution is the key, *ACS Catal.* 6 (2016) 6265–6274.
- [16] B. Kumar, M. Asadi, D. Pisasale, S. Sinha-Ray, B.A. Rosen, R. Haasch, J. Abiade, A.L. Yarin, A. Salehi-Khojin, Renewable and metal-free carbon nanofibre catalysts for carbon dioxide reduction, *Nat. Commun.* 4 (2013) 2819.
- [17] M. Asadi, B. Kumar, A. Behranginia, B.A. Rosen, A. Baskin, N. Reznin, D. Pisasale, P. Phillips, W. Zhu, R. Haasch, R.F. Klie, P. Král, J. Abiade, A. Salehi-Khojin, Robust carbon dioxide reduction on molybdenum disulphide edges, *Nat. Commun.* 5 (2014) 4470.
- [18] A. Roy, D. Hursán, K. Artyushkova, P. Atanassov, C. Janáky, A. Serov, Nanostructured metal-N-C electrocatalysts for CO₂ reduction and hydrogen evolution reactions, *Appl. Catal. B: Environ.* 232 (2018) 512–520.
- [19] W. Ju, A. Bagger, G.P. Hao, A.S. Varela, I. Sinev, V. Bon, B. Roldan Cuenya, S. Kaskel, J. Rossmeisl, P. Strasser, Understanding activity and selectivity of metal-nitrogen-doped carbon catalysts for electrochemical reduction of CO₂, *Nat. Commun.* 8 (2017) 944.
- [20] C. Yan, H. Li, Y. Ye, H. Wu, F. Cai, R. Si, J. Xiao, S. Miao, S. Xie, F. Yang, Y. Li, G. Wang, X. Bao, Coordinatively unsaturated nickel-nitrogen sites towards selective and high-rate CO₂ electroreduction, *Energy Environ. Sci.* 11 (2018) 1204–1210.
- [21] C.M. Zhao, X.Y. Dai, T. Yao, W.X. Chen, X.Q. Wang, J. Wang, J. Yang, S.Q. Wei, Y.E. Wu, Y.D. Li, Ionic exchange of metal organic frameworks to access single nickel sites for efficient electroreduction of CO₂, *J. Am. Chem. Soc.* 139 (2017) 8078–8081.
- [22] A. Han, W. Chen, S. Zhang, M. Zhang, Y. Han, J. Zhang, S. Ji, L. Zheng, Y. Wang, L. Gu, C. Chen, Q. Peng, D. Wang, Y. Li, A polymer encapsulation strategy to synthesize porous nitrogen-doped carbon-nanosphere-supported metal isolated-single-Atomic-Site catalysts, *Adv. Mater.* 30 (2018) 1706508.
- [23] Y. Chen, S. Ji, C. Chen, Q. Peng, D. Wang, Y. Li, Single-atom catalysts: synthetic strategies and electrochemical applications, *Joule* 2 (2018) 1242–1264.
- [24] M. Zhang, Y.-G. Wang, W. Chen, J. Dong, L. Zheng, J. Luo, J. Wan, S. Tian, W.-C. Cheong, D. Wang, Y. Li, Metal (hydr)oxides/polymer core-shell strategy to metal single-atom materials, *J. Am. Chem. Soc.* 139 (2017) 10976–10979.
- [25] S. Dilpazir, H. He, Z. Li, M. Wang, P. Lu, R. Liu, Z. Xie, D. Gao, G. Zhang, Cobalt single atoms immobilized N-doped carbon nanotubes for enhanced bifunctional catalysis toward oxygen reduction and oxygen evolution reactions, *ACS Appl. Energy Mater.* 1 (2018) 3283–3291.
- [26] H. Xiaochun, L. Yanyong, Z. Jiepeng, C. Xiaoming, Ligand-directed strategy for zeolite-type metal-organic frameworks: zinc(II) imidazolates with unusual zeolitic topologies, *Angew. Chem.* 118 (2006) 1587–1589.
- [27] F. Lei, W. Liu, Y. Sun, J. Xu, K. Liu, L. Liang, T. Yao, B. Pan, S. Wei, Y. Xie, Metallic tin quantum sheets confined in graphene toward high-efficiency carbon dioxide electroreduction, *Nat. Commun.* 7 (2016) 12697.
- [28] B. Jürgens, E. Irran, J. Senker, P. Kroll, H. Müller, W. Schnick, Melem (2,5,8-Triamino-tri-s-triazine), an important intermediate during condensation of melamine rings to graphitic carbon nitride: synthesis, structure determination by X-ray powder diffractometry, solid-state NMR, and theoretical studies, *J. Am. Chem. Soc.* 125 (2003) 10288–10300.